

# DispFormer: Pretrained Transformer for Flexible Dispersion Curve Inversion from Global Synthesis to Regional Applications

Feng Liu, Bao Deng, Rui Su, Lei Bai, Wanli Ouyang

**Abstract**—Surface wave dispersion curve inversion is essential for estimating subsurface Shear-wave velocity ( $v_s$ ), yet traditional methods often struggle to balance computational efficiency with inversion accuracy. While deep learning approaches show promise, previous studies typically require large amounts of labeled data and struggle with real-world datasets that have varying period ranges, missing data, and low signal-to-noise ratios. This study proposes DispFormer, a transformer-based neural network for inverting the  $v_s$  profile from Rayleigh-wave phase and group dispersion curves. DispFormer processes dispersion data at each period independently, thereby allowing it to handle data of varying lengths without requiring network modifications or alignment between training and testing data. The performance is demonstrated by pre-training it on a global synthetic dataset and testing it on two regional synthetic datasets using zero-shot and few-shot strategies. Results indicate that zero-shot DispFormer, even without any labeled data, produces inversion profiles that match well with the ground truth, providing a deployable initial model generator to assist traditional methods. When labeled data is available, few-shot DispFormer outperforms traditional methods with only a small number of labels. Furthermore, real-world tests indicate that DispFormer effectively handles varying length data, and yields lower data residuals than reference models. These findings demonstrate that DispFormer provides a robust foundation model for dispersion curve inversion and is a promising approach for broader applications.

**Index Terms**—dispersion curve inversion, Shear-wave velocity estimation, transformer neural network, zero-shot and few-shot learning

## I. INTRODUCTION

**S**URFACE wave tomography, which utilizes the cross-correlation functions of long-term seismic ambient noise [1]–[4] or surface waves generated by regional and global earthquakes [5]–[10], has proven to be a powerful method for investigating the interior of the Earth. This technique is widely used for high-resolution imaging of the crust and lower mantle [11]–[13], and is increasingly applied in near-surface exploration [14], [15]. A commonly used approach in surface wave tomography involves a two-step inversion process. In the first step, group and/or phase velocity maps are constructed across multiple periods. These maps are then

employed to generate dispersion curves for each grid cell, which are subsequently inverted to obtain one-dimensional (1-D) shear wave velocity ( $v_s$ ) profiles [16].

The inversion process that maps surface wave dispersion curves to a 1-D depth profile of  $v_s$  is inherently nonlinear and underdetermined [17], [18]. Conventional methods include linearized inversion techniques [19], which iteratively refine an assumed initial velocity model using gradient descent, and global search algorithms such as Monte Carlo [20], [21] and particle swarm optimization (PSO) [22], which explore a broad parameter space to identify optimal solutions. As the number of deployed seismic arrays and shared databases increases, the limitations of both approaches become more pronounced. Linearized inversion encounters difficulties in yielding accurate results without a good initial model, while global search algorithms face significant computational challenges [23], [24].

Deep learning has emerged as a promising alternative to traditional methods, offering a balance between efficiency and accuracy in various inversion applications, including gravity inversion [25], [26], electromagnetic inversion [27], [28], and seismic inversion [29], [30]. In the context of surface wave dispersion curve inversion, early studies used fully connected neural networks (FCNNs) to estimate surface wave velocities and layer thicknesses [31]–[33], paving the way for more advanced deep learning approaches. For example, Hu et al. [34] utilized convolutional neural networks (CNNs) to improve inversion results on two regional datasets from continental China and southern California. Earp et al. [35] and Yang et al. [36] employed mixture density networks to derive  $v_s$  structures while quantifying inversion uncertainty. Aleardi and Stucchi [37], along with Gan et al. [38], used residual networks (ResNets) to directly map the full dispersion spectrum to  $v_s$  models. Additionally, Luo et al. [39] trained a deep FCNN on a global synthetic dataset and validated its performance on regional datasets. Cai et al. [40] proposed a semi-supervised Cycle-GAN to enhance generalization in poorly constrained regions.

Despite these advancements, most existing network architectures are limited by the requirement for fixed-length dispersion data, which restricts their applicability to real-world scenarios where dispersion curves often face challenges such as inconsistent data ranges, missing data, and low signal-to-noise ratios [14], [41], [42]. Moreover, these models typically exhibit limited generalization capabilities, performing well on training datasets but underperforming on unseen or diverse

Feng Liu is with the School of Electronic Information and Electrical Engineering, Shanghai Jiao Tong University, Shanghai 200240, China, and also with Shanghai Artificial Intelligence Laboratory, Shanghai 200232, China. Bao Deng is with the Laboratory of Seismology and Physics of Earth's Interior, School of Earth and Space Sciences, University of Science and Technology of China, 96 Jinzhai Road, Hefei 230026 Anhui, China. Rui Su, Lei Bai, and Wanli Ouyang are with the Shanghai Artificial Intelligence Laboratory, Shanghai 200232, China (email: surui@pjlab.org.cn). Codes and data are available at <https://github.com/liufeng2317/DispFormer>

datasets [34], [38]. In practice, applying these models often requires large labeled datasets for case-specific training and the alignment of training and observed data through methods such as cropping, interpolation, or padding. However, large labeled datasets and length-aligned observations are rarely available in surface wave dispersion curve inversion studies. These challenges underscore the need for more robust and adaptable methods that can accommodate varying lengths and deliver reliable results across a broad range of datasets.

To address these challenges, this study introduces three primary contributions: 1) DispFormer, a transformer-based network for varying-length dispersion data. The model encodes dispersion data using linear layers and position embeddings, extracts period-related features through multiple transformer blocks, and finally projects the results into a 1-D velocity profile. 2) Pre-training and zero-shot testing: DispFormer is pre-trained on a global synthetic dataset to embed prior knowledge of surface wave dispersion. Tests on regional datasets demonstrate that the pre-trained model effectively handles varying-length dispersion data and generalizes well to unseen datasets. Using this prior knowledge, zero-shot DispFormer provides a plug-and-play solution for generating reliable initial models in traditional inversion workflows. 3) Few-shot testing: When a small amount of labeled data is available, fine-tuning the pre-trained DispFormer significantly improves performance. Both synthetic and real-world tests show that the fine-tuned model produces inversion results that are comparable to, or even exceed, those of traditional global search methods.

## II. METHODOLOGY

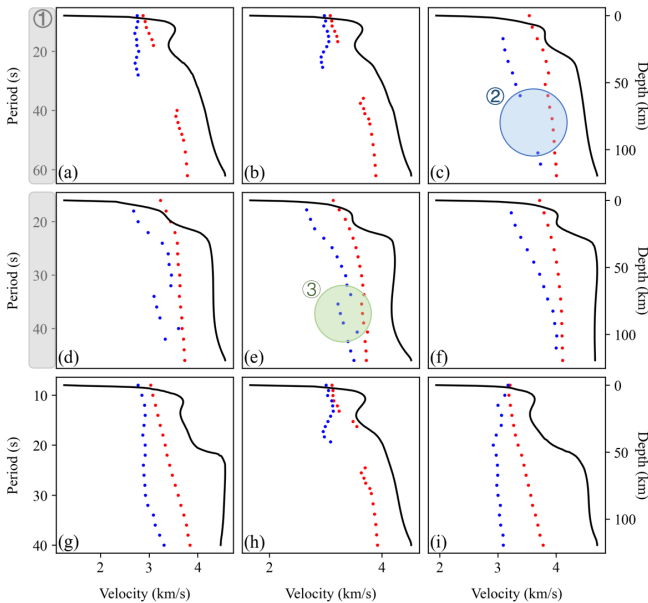


Fig. 1. Examples of real dispersion curves and corresponding S-wave velocity profile derived from the China Seismological Reference Model. The black line indicate the 1-D S-wave velocity profiles with thickness of 0.5 km range from 0 to 120 km. The blue and red scatters indicate the observed phase and group dispersion data. Remarkable features of the real dispersion curves are specifically labeled in the figure, including (1) varying period ranges, (2) missing data, and (3) lower signal-to-noise ratios.

### A. Theory of Dispersion Curve Inversion

For a horizontally layered Earth model, the forward modeling of the Rayleigh wave dispersion curves can be expressed as [43], [44]:

$$\mathbf{d}(\tau) = G(v_p, v_s, \rho, h), \quad (1)$$

where  $G$  is the forward operator that takes the layered earth model as input, including P-wave velocity ( $v_p$ ), S-wave velocity ( $v_s$ ), density ( $\rho$ ), and layer thickness ( $h$ ) for each layer. The output of this operation,  $\mathbf{d}(\tau)$ , corresponds to the dispersion data at a given period  $\tau$ , which includes both phase and group velocities.

Inversion aims to estimate the underlying Earth model parameters based on observed dispersion data. Traditional inversion methods can be broadly categorized into linearized and global approaches. Linearized inversion iteratively refines an initial model, typically using gradient-based optimization to minimize the discrepancy between observed and modeled data [17], [19]. However, its effectiveness heavily depends on the quality of the initial model; a well-chosen starting model increases the likelihood of convergence to the global minimum, while a poor choice raises the risk of being trapped in a local minimum [45]. Global search algorithms, in contrast, explore the parameter space more comprehensively to identify the optimal model. These methods are less dependent on initial guesses and are generally more robust but come with substantial computational costs, which limits their practicality for large-scale applications.

To achieve a balance between efficiency and accuracy in inversion, deep learning techniques have been increasingly employed to learn the nonlinear mappings between dispersion curves and S-wave velocity [38], [46], which can be mathematically expressed as:

$$\mathbf{m} = f(\mathbf{d}; \theta) \quad (2)$$

where  $f$  denotes the neural network, parameterized by  $\theta$ . The input to the neural network,  $\mathbf{d}$ , consists of phase and/or group velocity dispersion data. The output,  $\mathbf{m} = [v_p, v_s, \rho, \mathbf{h}]$ , represents the predicted subsurface velocity model. In practice, empirical relationships are often used to estimate  $v_p$  and  $\rho$  due to their relatively low sensitivity to Rayleigh wave dispersion data [17]. Additionally, the layers can be divided into thin layers of equal thickness to standardize the output of the network [34], [40], [47]. These simplifications allow the inversion process to focus on  $v_s$ , the primary variable of interest for surface wave tomography.

Supervised learning techniques are then used to train the neural network by minimizing the discrepancy between the predicted and true velocity models. This process is achieved through the following misfit functions:

$$\mathcal{J}(\mathbf{d}, \mathbf{m}; \theta) = \frac{1}{N} \sum_{i=1}^N \mathcal{L}(f(d_i; \theta), \mathbf{m}_i) \quad (3)$$

where  $\mathcal{J}$  denotes the misfit function,  $N$  represents the number of samples,  $f(\mathbf{d}_i; \theta)$  is the predicted velocity model for the  $i$ -th input dispersion data  $\mathbf{d}_i$ , and  $\mathbf{m}_i$  is the corresponding true velocity model. The function  $\mathcal{L}(\cdot, \cdot)$  quantifies the difference

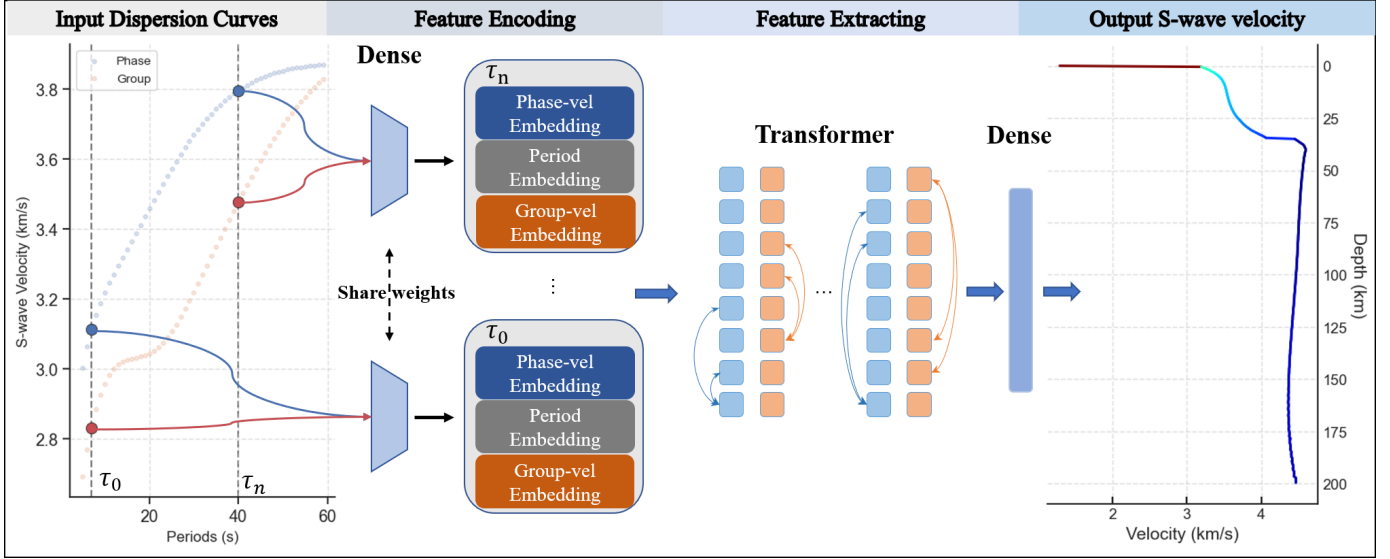


Fig. 2. Architecture of the DispFormer network. The network takes dispersion curves, including period, phase velocity, and group velocity, as inputs. Each period of the dispersion data is encoded using linear layers combined with positional embeddings to retain temporal relationships. Transformer blocks are then employed to model inter-period correlations. Finally, the extracted features are projected through a dense layer to estimate the shear-wave velocity ( $v_s$ ) at fixed depths.

between the predicted and true velocity models, typically using metrics such as mean squared error (MSE) or mean absolute error (MAE). Once trained, the neural network can efficiently conduct inversion mapping without requiring iterative optimization or extensive random sampling, which are common in traditional methods.

### B. DispFormer for Arbitrary-length Dispersion Data

Previous studies have successfully applied various neural networks, such as FNNs, CNNs, and ResNets, to learn the inversion mapping between dispersion curves and S-wave velocity profile. However, the intrinsic characteristics of the dispersion data present challenges for training a universal neural network that can adapt to diverse real-world scenarios. A critical factor is the varying period ranges, which are directly related to the depth of the inversion, as longer periods typically provide information about deeper structures [14], [48]. Notably, period ranges can vary significantly across different study areas, and even within a single dataset, the dispersion curves may exhibit distinct effective ranges. Additionally, some dispersion curves may have a lower signal-to-noise ratios, while others may contain missing data due to limitations in the data acquisition and picking processes. As shown in Fig. 1, observed dispersion curves often feature varying ranges, missing data, and low signal-to-noise ratio. Consequently, neural network architectures that rely on fixed-length input data may struggle to accommodate these variations.

In this study, we propose DispFormer, a transformer-based architecture designed to handle dispersion data of arbitrary length. Fig. 2 illustrates the workflow of DispFormer, where the dispersion curves are used as input and the corresponding S-wave velocity at each depth is generated as output. Initially, dense layers separately encode the period, phase velocity, and group velocity for each period. To preserve the relative

distances between periods, additional position embeddings are incorporated. Transformer blocks are then employed to capture the relationships between different periods of the surface wave dispersion curves, which are essential for modeling the depth-dependent velocity structure. Finally, a dense layer maps the extracted features to the S-wave velocity. The flexibility of DispFormer in handling data of arbitrary length is achieved through two strategies: encoding each period of data independently and leveraging the transformer architecture, which supports inputs of varying lengths.

### C. Workflow for Pre-training and Fine-tuning DispFormer

The capability of DispFormer to accommodate dispersion data of arbitrary length facilitates the implementation of a pre-training and fine-tuning strategy, significantly enhances its generalization ability. In this study, a global synthetic dataset was created for pre-training. This dataset, with spatial resolution of approximately  $1^\circ$  and period ranges spanning from 1 to 100 seconds, is designed to capture crust and upper mantle structures down to depths of about 200 km (Fig. 3a). The resulting pre-trained model provides a robust foundation for subsequent applications.

In regional studies with higher spatial resolutions (e.g.,  $< 0.25^\circ$ ) and varying period ranges (e.g., 10-60 s, 8-80 s), the pre-trained DispFormer can be directly applied to map observed dispersion curves to S-wave velocity, even in the absence of labeled data. This "zero-shot" strategy (Fig. 3b) eliminates the need for region-specific training, offering an efficient solution for generating initial models. While the inversion results may not always outperform those of traditional global search methods due to the domain gap between pre-training dataset and regional observation datasets, the velocity models generated by the pre-trained DispFormer remain highly valuable. They can serve as practical initial models or provide

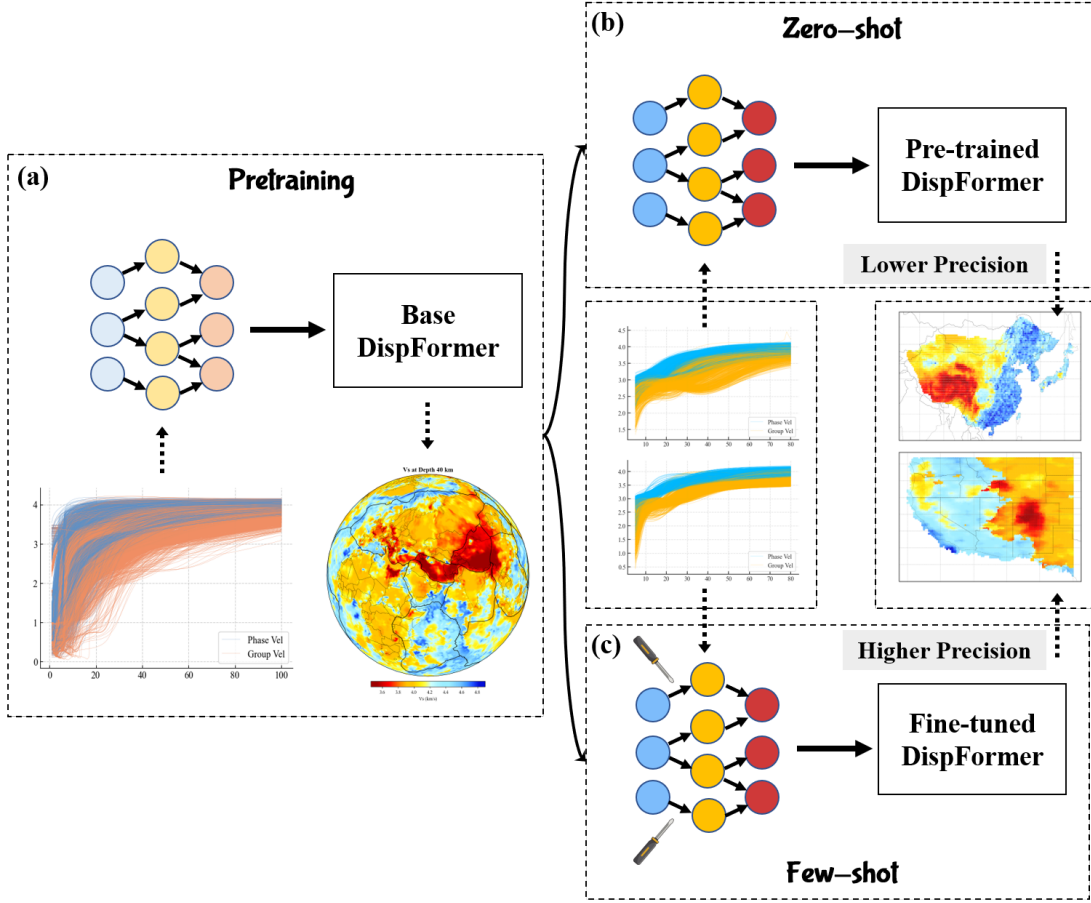


Fig. 3. Workflow of DispFormer pre-training and utilization strategies. (a) Pre-training process using a global synthetic dataset to train the model for general inversion tasks. (b) Zero-shot inversion using the pre-trained model applied directly to regional datasets without labeled data. (c) Fine-tuning process, where a small amount of labeled data is used to adapt the pre-trained model, improving accuracy on specific regional datasets.

meaningful constraints for subsequent inversion processes. In this way, DispFormer functions as a plug-and-play tool to support and enhance traditional inversion techniques.

When labeled data, such as well logs or results from global searches, are available, the pre-trained model can be fine-tuned to better align with the regional data distribution. This "few-shot" strategy (Fig. 3c) requires only a small subset of labeled data, yet it significantly enhances inversion accuracy. Remarkably, fine-tuned DispFormer achieves inversion results that are comparable to, or even surpass, those of traditional global search methods.

#### D. Training and Testing Process

During the training process, DispFormer iteratively minimizes the misfit function,  $\mathcal{J}$ , by adjusting the model parameters,  $\theta$ . Since the velocity varies with depth, the misfit function is defined as the normalized mean squared error (NMSE), which accounts for variations in the relative velocity scale. The NMSE is expressed as [49]:

$$\mathcal{L}(f(\mathbf{d}; \theta), \mathbf{m}) = \frac{1}{N} \sum_{i=1}^N \left( \frac{f(\mathbf{d}_i; \theta) - \mathbf{m}_i}{\mathbf{m}_i} \right)^2 \quad (4)$$

where  $N$  denotes the number of samples in the training dataset, and  $\mathbf{m}_i$  and  $f(\mathbf{d}; \theta)$  represent the true and predicted velocity models for the  $i$ -th sample, respectively.

For optimization, the adaptive moment estimation (Adam) optimizer [50] is employed, with an initial learning rate of  $1 \times 10^{-4}$  during pre-training, and subsequently reduced to  $5 \times 10^{-5}$  during fine-tuning. A step-based learning rate decay scheduler (StepLR) is incorporated to automatically adjust the learning rate as training progresses, thereby improving convergence and stability.

To evaluate the predictive performance, the mean absolute error (MAE) is defined as:

$$\text{MAE} = \frac{1}{N} \sum_{i=1}^N |f(\mathbf{d}_i; \theta) - \mathbf{m}_i|. \quad (5)$$

### III. DATA: SYNTHETIC AND REAL

#### A. Global Synthetic Data for Pre-training

The pre-training datasets used in this study are entirely synthetic, constructed from an extensive collection of 1-D velocity profiles. To capture diverse and realistic features, a paired global velocity-dispersion dataset is first created based on the updated Earth crust and lithosphere model (LITHO1.0) [51]. The fundamental mode Rayleigh-wave phase and group



velocity are computed from these extracted velocity profiles, and the construction process is outlined as follows:

- 1) Initially, 40,962 1-D S-wave velocity profiles, extending to a depth of 200 km, are extracted from the LITHO1.0 database. Any water layers in the profiles are removed, and each profile is then converted into an isothermal layer model with a uniform layer thickness of 0.5 km, using linear interpolation.
- 2) Given the relatively low sensitivity of Rayleigh wave phase and group velocities to  $v_p$  and  $\rho$ ,  $v_p$  for depths above 120 km is computed from  $v_s$  using the empirical relationships established by Brocher [52], with a fixed  $v_p/v_s$  ratio of 1.79 for depths between 120 and 200 km [53]. Additionally,  $\rho$  is derived from  $v_p$  using Brocher's empirical relationship [52].
- 3) Theoretical Rayleigh wave phase and group velocity dispersion curves for periods ranging from 1 to 100 seconds are generated using the Computer Programs in Seismology (CPS) software package [19]. To ensure comprehensive coverage of real-world scenarios, periods are drawn not only uniformly at integer period positions but also logarithmically and randomly within the period domain [47].
- 4) During the pre-training phase, the complete dataset is used to train the model, and the best optimized model is selected as the base model. To improve the generalization and stability of the base model, several data augmentation strategies are introduced, including: a) adding random Gaussian noise (approximately 5%), b) zeroing out random segments of the data (approximately 10%), and c) randomly removing either phase velocity or group velocity.
- 5) Considering that dispersion curves with varying period ranges are sensitive to different depth ranges, a dynamic calculation approach is adopted to determine the approximate depth range based on the wavelengths of observed dispersion curves. The calculation can be formulated as:

$$z_{min} = \min(C_1\lambda_p, C_2\lambda_g), \quad (6)$$

$$z_{max} = C_3 \max(\lambda_p, \lambda_g), \quad (7)$$

where  $z_{min}$  and  $z_{max}$  represent the minimum and maximum sensitive depths, respectively. The phase and group wavelengths for each period  $\tau_i$  are given by  $\lambda_p^i = v_{phase}^i \times \tau_i$  and  $\lambda_g^i = v_{group}^i \times \tau_i$ , where  $v_{phase}^i$  and  $v_{group}^i$  are the phase and group velocities. The constants  $C_1$ ,  $C_2$ , and  $C_3$  are empirical scaling factors, with values of  $C_1 = 1/3$ ,  $C_2 = 1/2$ , and  $C_3 = 1.1$  used in this study.

### B. Regional Synthetic Data for Model Validation

To evaluate the stability and performance of DispFormer, two regional synthetic datasets are generated based on the S-wave velocity profiles from Shen et al. [54] and Shen et al. [55]. The dataset from Shen et al. [54] consists of 6,803 1-D S-wave velocity profiles derived from a tomographic model of the central and western United States, while Shen et al.

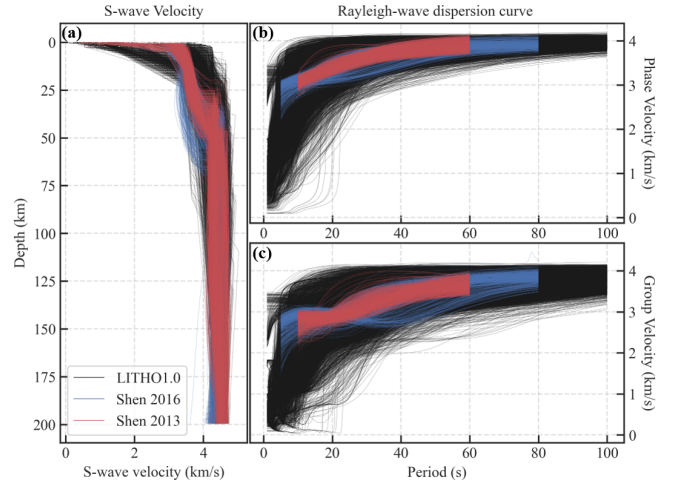


Fig. 4. Distribution of the global and local synthetic datasets. (a) S-wave velocity profiles, with the black, red, and blue curves representing data from LITHO1.0, Shen et al. (2013) [54], and Shen et al. (2016) [55], respectively; (b) distribution of Rayleigh-wave phase velocity dispersion curves; (c) distribution of Rayleigh-wave group velocity dispersion curves.

[55] provides 4,527 profiles from continental China. These datasets are herein referred to as the Central and Western US Dataset (CWD) and the Continental China Dataset (CCD), respectively. The thickness, P-wave velocity and density for both datasets are calculated using the same parametrization strategy as that employed for the pre-training dataset. The dispersion periods are sampled at 1-second intervals, spanning 10 to 60 s for the CWD and 5 to 80 s for the CCD, providing distinct period ranges compared to the pre-training data.

When testing DispFormer on these synthetic datasets, the zero-shot strategy allows direct evaluation without requiring any training data. In contrast, the few-shot strategy involves selecting a small subset (less than 2%) of the regional dataset for fine-tuning, done through a hierarchical selection process. The distribution of the global and regional synthetic datasets is illustrated in Fig. 4.

### C. Field Data for Model Testing

Xiao et al. [56] propose a high-resolution China Seismological Reference Model (CSRМ) by integrating various seismic data, with extensive surface wave dispersion data being used to derive the S-wave velocity. The dispersion data, spanning periods from 8 to 70 seconds, are extracted from three-component waveforms of 9,361 teleseismic events recorded at 4,193 seismic stations across mainland China. These observations are mapped onto a regular grid, with finer resolution of  $0.2^\circ \times 0.2^\circ$  for the North-South Seismic Belt and the trans-North China orogen regions, and coarser resolution of  $0.4^\circ \times 0.4^\circ$  for the remainder of the continent.

For this study, 12,705 observed dispersion curves are extracted from the original CSRМ database and directly used to construct the test dataset. Fig. 1 presents examples of the observed dataset, which exhibit issues such as varying period ranges, missing data, and low signal-to-noise ratios. Additionally, the corresponding reference velocity profiles are

interpolated into 0.5 km thick layers, with a maximum depth of 120 km.

#### IV. APPLICATION AND VERIFICATION

##### A. Zero-shot Generation of Reasonable Initial Models

This section conducts zero-shot tests on two regional synthetic datasets using the pre-trained DispFormer. Since DispFormer is designed to process dispersion data of arbitrary length, the model directly ingests dispersion curves from the CWD and CCD datasets, with period ranges of 10 to 60 s for CWD and 5 to 80 s for CCD, to obtain the corresponding inverted S-wave velocity profiles.

Fig. 5 shows slices of the true and inverted S-wave velocity models at depths of 20, 40, 50, and 90 km, derived from the CWD dataset. The first column (Figs. 5a, e, i, and m) displays the target velocity model, while the second column shows the interpolated model obtained from the LITHO1.0 database, which is also used for pre-training the DispFormer model. The third column presents the inversion results from the pre-trained DispFormer with zero-shot strategy. The final column illustrates the error distributions between the target model and both the interpolated LITHO1.0 model and the zero-shot DispFormer’s results. This highlights that the error distribution for the zero-shot DispFormer is much more tightly centered around zero, with fewer large error samples compared to the interpolated model.

Furthermore, the Continental China dataset, with its broader period range, enables the inversion of S-wave velocities at greater depths. Fig. 6 shows the true and inverted results at depths of 30, 55, 100, and 170 km based on this dataset. The results clearly demonstrate that the zero-shot DispFormer more accurately captures the lower-velocity anomalies in the Tibetan Plateau area.

Table I summarizes the MAE between the target model and both the interpolated LITHO1.0 model and the inverted results from the zero-shot DispFormer for CWD and CCD datasets. The results demonstrate that the zero-shot DispFormer consistently outperforms the interpolated model at all tested depths. Notably, the interpolated model is commonly used to construct the initial velocity model or define the upper and lower boundaries for traditional inversion processes. Therefore, the zero-shot DispFormer provides a robust, plug-and-play alternative for generating initial models in traditional inversion frameworks.

TABLE I

MEAN ABSOLUTE ERROR OF THE INTERPOLATED LITHO1.0 MODEL AND THE ZERO-SHOT DISPFORMER ON THE CWD AND CCD DATASETS.

	Interped LITHO1.0	zero-shot DispFormer
CWD	234.53 m/s	<b>72.78 m/s</b>
CCD	233.61 m/s	<b>73.27 m/s</b>

##### B. Few-shot DispFormer for Improved Results

The adaptability of a pre-trained DispFormer model to local datasets can be further enhanced through fine-tuning when

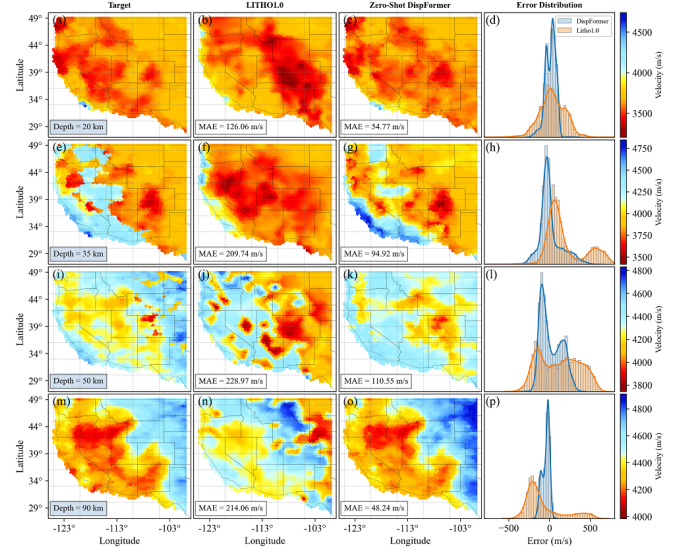


Fig. 5. Comparison of S-wave velocity models at depths of 20, 40, 50, and 90 km using the CWD dataset. Columns show (1) target velocity model, (2) interpolated LITHO1.0 model, (3) inverted result from zero-shot DispFormer, and (4) error distributions relative to the target model.

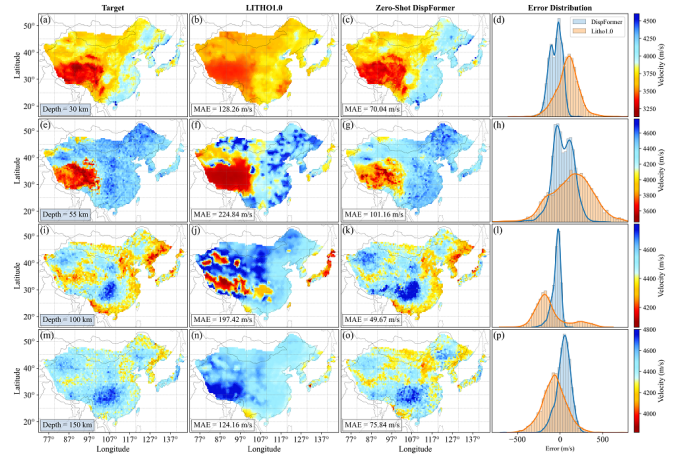


Fig. 6. Comparison of S-wave velocity models at depths of 30, 55, 100 and 170 km using the CCD dataset. Columns show (1) target velocity model, (2) interpolated LITHO1.0 model, (3) inverted result from zero-shot DispFormer, and (4) error distributions relative to the target model.

labeled data is accessible. To evaluate the effectiveness of few-shot learning, experiments are carried out on two regional datasets. The inversion results obtained by fine-tuning with limited labeled data are contrasted with those from a global search algorithm. For the global search baseline, a particle swarm optimization (PSO) algorithm is implemented [57], with a search range of  $\pm 0.6$  km around the true velocity model and an iteration limit of 2000.

Fig. 7 compares the inverted S-wave velocity models obtained from the PSO and few-shot DispFormer at depths of 20, 40, 50, and 90 km using the CWD dataset. The first column shows the true S-wave velocity model, while the second column presents the inversion results using the PSO method. The third and fourth columns display the inverted results from the few-shot DispFormer, fine-tuned with 10 and



108 labeled samples, respectively. Similarly, Fig. 8 provides a comparison using the CCD dataset, with fine-tuning performed using 36 and 180 labeled samples.

Table II summarizes the MAE between the target velocity model and the inversion results from the PSO global search method and few-shot DispFormer. These results demonstrate that the few-shot DispFormer, which uses only a minuscule number of labeled samples (e.g. 10 for CWD and 36 for CCD) for fine-tuning, achieves inversion results comparable to those from the global search method. Furthermore, when hundreds of labeled samples are available, the fine-tuned DispFormer outperforms the global search method. These findings highlight the potential of few-shot DispFormer to efficiently generate high-quality inversion models, even with limited labeled data, rendering it highly valuable for practical applications where labeled data is scarce.

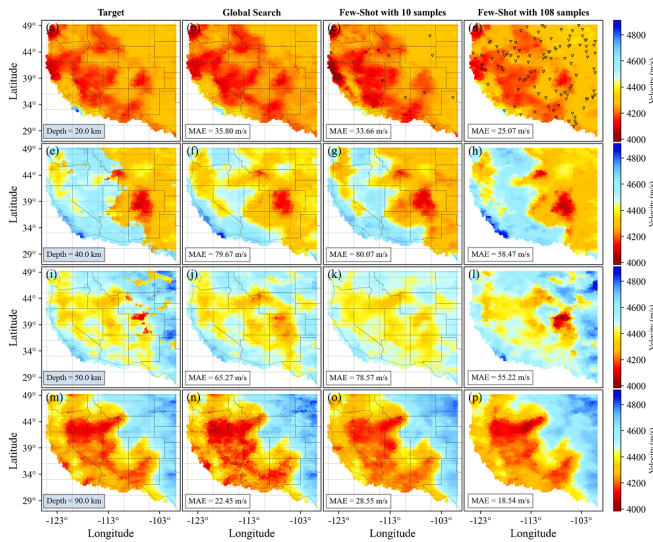


Fig. 7. Comparison of inverted S-wave velocity models at depths of 20, 40, 50, and 90 km using the CWD dataset. Columns show: (1) target velocity model, (2) PSO global search results, (3) fine-tuned DispFormer with 10 samples, and (4) fine-tuned DispFormer with 108 samples.

TABLE II

MEAN ABSOLUTE ERROR OF THE PSO AND THE FEW-SHOT MODELS ON THE CWD AND CCD DATASETS. THE NUMBERS IN PARENTHESES INDICATE THE NUMBER OF DATA USED FOR FINE-TUNING, RESPECTIVELY.

	PSO	Few-shot DispFormer (10 CWD / 36 CCD)	Few-shot DispFormer (108 CWD / 180 CCD)
CWD	42.77 m/s	45.70 m/s	<b>33.84 m/s</b>
CCD	36.87 m/s	36.58 m/s	<b>28.69 m/s</b>

### C. Field Case

The use of real-world dispersion data presents several challenges, including varying period ranges, missing data, and low signal-to-noise ratios (fig. 1). Traditional deep learning-based inversion frameworks usually require alignment between observation and training datasets, which hinders the application of models trained on one dataset to others. In contrast,

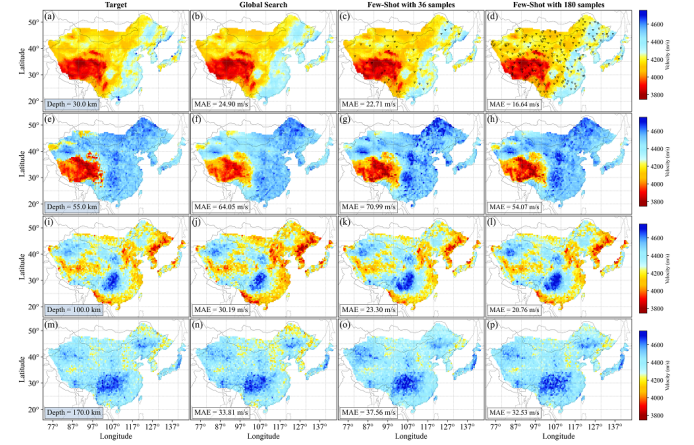


Fig. 8. Comparison of inverted S-wave velocity models at depths of 30, 55, 100, and 170 km using the CCD dataset. Columns show: (1) target velocity model, (2) PSO global search results, (3) fine-tuned DispFormer with 36 samples, and (4) fine-tuned DispFormer with 180 samples.

DispFormer is specifically designed to handle data of arbitrary length, making it adaptable to datasets with varying period ranges. Furthermore, DispFormer improves its generalization capability by integrating pre-training, fine-tuning, and data augmentation techniques. These features make DispFormer particularly suitable for real-world data applications.

To evaluate the performance of DispFormer, the pre-trained model was tested via both zero-shot and few-shot approaches on the CSRM dataset. The slices of the reference model and inverted results at depths of 10, 40, 60, and 100 km are shown in Fig. 9. The first column displays the reference model from Xiao et al. [56], while the second column shows the inversion results using zero-shot DispFormer. The third and fourth columns present the results after fine-tuning with 38 and 114 labeled samples, respectively. It should be noted that the velocity profiles used for fine-tuning were randomly selected from the reference model, and the corresponding dispersion curves were synthesized using the CPS program. The MAE between the inversion results and the reference model are shown in the lower left of each sub-figure. The results demonstrate that zero-shot DispFormer can accurately replicate the reference model, capturing large-scale anomalies such as the low-velocity zone of the Tibetan Plateau. Furthermore, fine-tuning with as little as 1% labeled data significantly enhances accuracy, particularly in resolving finer structural details.

In real data applications, since there is no true model available for direct comparison, the accuracy of inversion results is typically assessed by calculating the data residuals between synthetic dispersion curves derived from the inversion results and the actual observed dispersion curves. To this end, Fig. 10 compares the data residual distributions for the CSRM reference model, zero-shot DispFormer, and Few-shot DispFormer (fine-tuned with 114 labeled samples). The comparison reveals that the inversion results from zero-shot DispFormer closely match the data domain of the CSRM reference model, while Few-shot DispFormer shows even greater alignment with the observed data. This ability to handle the complexities of real-world datasets highlights the potential of DispFormer

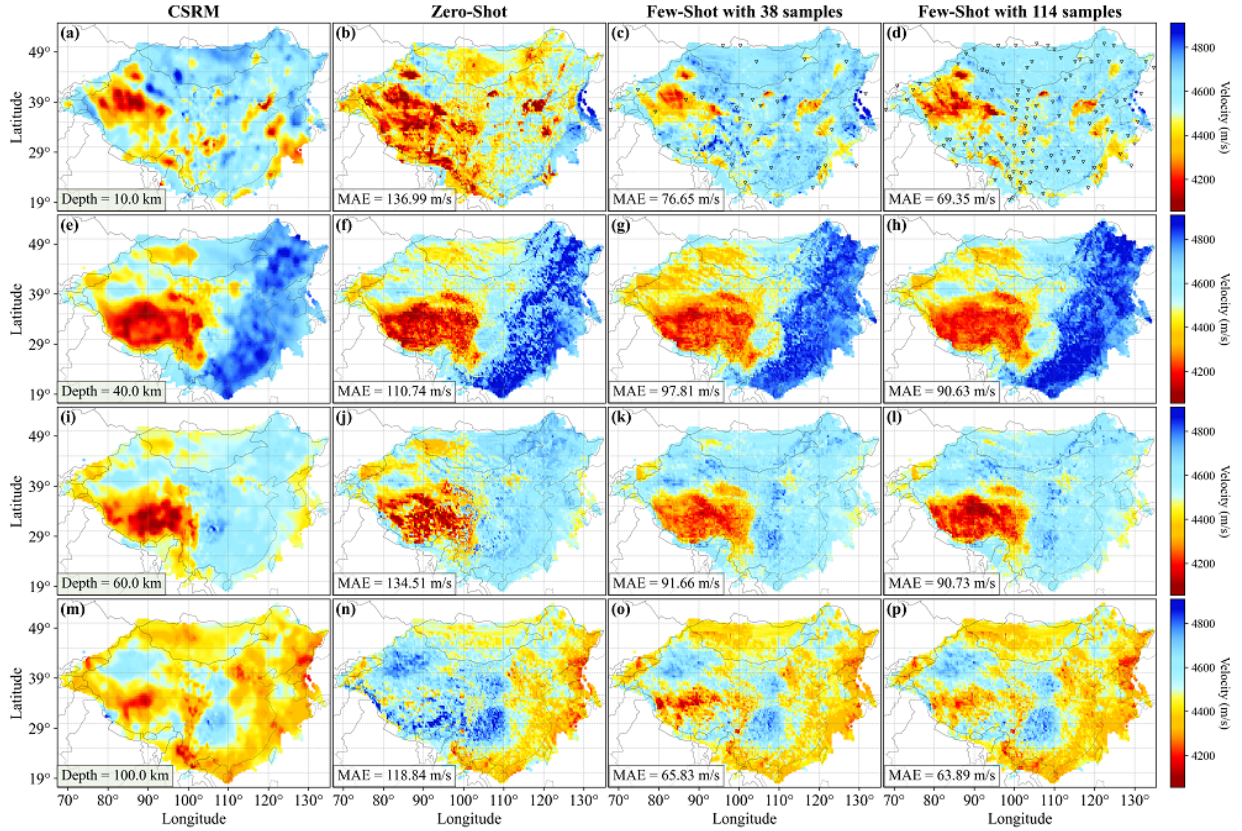


Fig. 9. Comparison of the reference model and inverted results using zero-shot and few-shot DispFormer at depths of 10, 45, 60, and 100 km with the CSRM dataset. Columns show: (1) reference model from CSRM, (2) zero-shot DispFormer, (3) fine-tuned DispFormer with 38 samples, and (4) fine-tuned DispFormer with 114 samples.

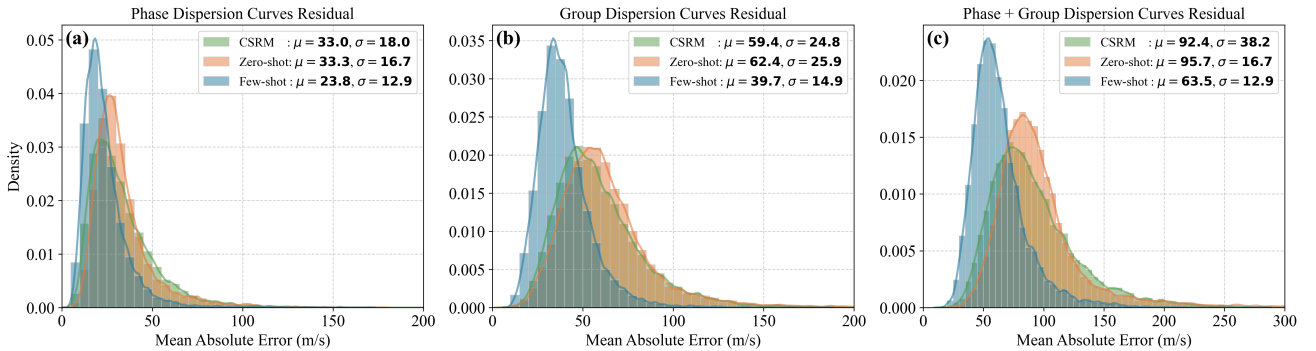


Fig. 10. Comparison of data residuals between observed dispersion curves and those synthesized from the reference model, zero-shot DispFormer, and Few-shot DispFormer inversion results. (a) the phase velocity error distribution, (b) the group velocity error distribution, and (c) the combined error distribution of both phase and group velocities.

as a robust and adaptable tool for large-scale geophysical inversions in diverse applications.

## V. DISCUSSION

### A. Impact of Depth Alignment Strategy

The depth alignment strategy employed during training dynamically aligns the period ranges of the dispersion curves with their corresponding sensitivity depths, thereby significantly improving the zero-shot performance of DispFormer. This strategy relies on empirical formulas for  $z_{min}$  and  $z_{max}$  to compute the inversion depth range, allowing the model

to capture depth-specific features which is consistent with the physical sensitivity of the observed dispersion data. In traditional deep learning methods, fixed inversion depths are commonly utilized. However, these may not align effectively with the specific depths sensitive to the observed data. As a consequence, this can potentially hinder the model's performance when applied to regional datasets. In contrast, by dynamically calculating the range of inversion depths, this strategy narrows the solution space and allows the model to learn more relevant features. As shown in Table III, a comparison of the MAE between zero-shot DispFormer mod-



els trained with and without depth alignment demonstrates that the alignment strategy consistently results in lower MAE across two regional synthetic datasets. By embedding physical constraints into the training process, this strategy not only improves the generalization ability of the network, but also highlights the importance of physics-informed preprocessing in data-driven inversion frameworks.

TABLE III  
MEAN ABSOLUTE ERROR COMPARISON OF ZERO-SHOT DISPFORMER WITH AND WITHOUT DEPTH ALIGNMENT FOR THE CWD AND CCD DATASETS.

	zero-shot (w/o Depth-Align)	zero-shot (w/ Depth-Align)
CWD	98.53 m/s	<b>72.78</b> m/s
CCD	91.20 m/s	<b>73.27</b> m/s

### B. Impact of noise

The synthetic tests discussed earlier demonstrate that, under ideal conditions with clean data, Few-shot DispFormer can be fine-tuned with a limited dataset to achieve inversion results that outperform traditional methods. However, in practical applications, real-world data is often contaminated by noise, which can affect the performance and stability of inversion models. To assess its robustness, we introduced Gaussian white noise with a standard deviation ranging from 0 % to 10 % of the observed dispersion curves on two regional synthetic datasets. Table IV presents the MAE for the inversion results obtained from the fine-tuned DispFormer across varying noise levels. The results indicate that, although the MAE increases as noise levels rise, the overall change remains moderate, with errors staying below 20 m/s. These findings underscore that DispFormer can deliver accurate and stable inversion results even in the presence of noise.

TABLE IV  
MEAN ABSOLUTE ERROR COMPARISON OF ZERO-SHOT DISPFORMER UNDER GAUSSIAN NOISE ON CWD AND CCD DATASETS

Few-Shot Samples	Noise Level	0%	2%	5%	8%	10%
	CWD with 10 samples	<b>45.7</b>	46.0	47.6	50.6	53.1
CWD with 108 samples	<b>33.8</b>	35.1	40.2	47.4	52.6	
CCD with 36 samples	<b>36.5</b>	37.2	40.3	45.5	49.9	
CCD with 180 samples	<b>28.7</b>	29.7	34.0	40.9	46.5	

### C. Uncertainty Estimation

Observed dispersion curves often contain significant errors due to the influence of environmental noise during data acquisition and the subjectivity involved in manual dispersion curve picking. These errors, already present in manual dispersion curve, can propagate into the inversion results, affecting their reliability. Assessing the impact of data uncertainty on inversion outcomes is therefore a crucial aspect of inversion research [58], [59]. A commonly used method for uncertainty estimation is Bayesian inversion, which incorporates uncertainty directly into the inversion process [60], [61]. However,

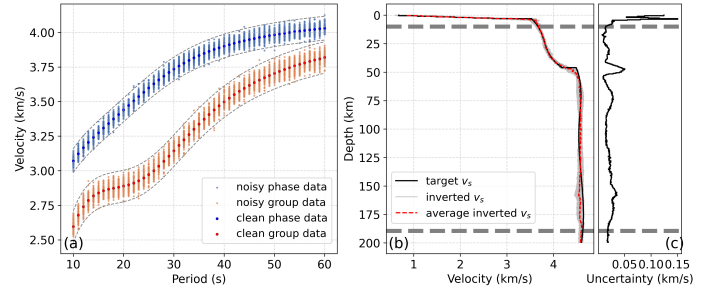


Fig. 11. Uncertainty estimation by perturbing observed data at a single station from the CWD datasets. (a) Clean and noisy dispersion curves, with noisy data generated by adding Gaussian white noise at 10 % standard deviation to the observed curves, repeated 1000 times. (b) Monte Carlo-based uncertainty estimation, the silver line shows the inverted  $v_s$  using the fine-tuned DispFormer, the red line represents the averaged inverted results, and the black line denotes the ground truth. (c) Estimated uncertainty (standard deviation) for each layer.

this approach tends to be computationally expensive. Another widely used method is the Monte Carlo-based approach, which transfers data errors from the data space to the model space by sampling and performing multiple inversions [6], [20], [62].

Monte Carlo-based methods require a large number of sampling and inversions, leading to high computational costs and time consumption in traditional approaches. In contrast, end-to-end deep learning methods like DispFormer are much more efficient in this regard. For a trained DispFormer, thousands of mappings can be performed in seconds, making it highly suitable for uncertainty assessment. To demonstrate this, we applied DispFormer to assess the uncertainty of inversion results at one station from the CWD datasets. In this example, the few-shot DispFormer was fine-tuned with 108 samples, and the test dataset was generated by adding random Gaussian white noise (10 % standard deviation) to the observed data, repeated 1,000 times. The clean and noisy data samples are shown in Fig. 11a, the inversion results are presented in Fig. 11b, and the estimated uncertainty is illustrated in Fig. 11c. Despite the significant error range in the observed data, the inversion results from DispFormer remain concentrated in a narrow range, and the average inversion result closely matches the true model.

## VI. CONCLUSION

This study introduces DispFormer, a transformer-based neural network designed to invert  $v_s$  models from Rayleigh-wave phase and/or group dispersion curves. DispFormer processes the dispersion data for each period independently, extracting period-related features via transformer blocks and subsequently mapping these features to  $v_s$  profile. The specially designed architecture supports dispersion data of arbitrary length, making it directly applicable to real-world datasets with varying lengths, without requiring adjustments to the network structure or alignment of training and test data.

To evaluate its performance, DispFormer is first pre-trained on the global synthetic LITHO1.0 dataset and then applied to two regional synthetic datasets in both zero-shot and few-shot modes. The synthetic tests demonstrate that the performance of zero-shot DispFormer is very close to that of traditional

global search methods, making it a reliable tool for generating high-quality initial models. Furthermore, when fine-tuned with limited labeled data, DispFormer achieved even better performance. Both synthetic and real data tests show that the few-shot mode of DispFormer outperforms traditional global search methods, delivering comparable or superior results with limited labeled data. Additionally, the real case study further highlights the versatility and high generalizability of DispFormer, which can be easily applied to complex datasets with varying period ranges, missing data, and low signal-to-noise ratios.

In summary, DispFormer, with its zero-shot capability for generating improved initial models and few-shot fine-tuning for superior inversion results, presents a promising approach for broader applications in surface wave tomography.

## REFERENCES

- [1] N. M. Shapiro, M. Campillo, L. Stehly, and M. H. Ritzwoller, "High-resolution surface-wave tomography from ambient seismic noise," *Science*, vol. 307, no. 5715, pp. 1615–1618, 2005.
- [2] H. Yao, R. D. Van Der Hilst, and M. V. De Hoop, "Surface-wave array tomography in se tibet from ambient seismic noise and two-station analysis - i. phase velocity maps," *Geophysical Journal International*, vol. 166, no. 2, pp. 732–744, 2006.
- [3] K. Nishida, J.-P. Montagner, and H. Kawakatsu, "Global surface wave tomography using seismic hum," *Science*, vol. 326, no. 5949, pp. 112–112, 2009.
- [4] K. Sager, L. Ermert, C. Boehm, and A. Fichtner, "Towards full waveform ambient noise inversion," *Geophysical Journal International*, vol. 212, no. 1, pp. 566–590, 2018.
- [5] J.-P. Montagner and T. Tanimoto, "Global anisotropy in the upper mantle inferred from the regionalization of phase velocities," *Journal of Geophysical Research: Solid Earth*, vol. 95, no. B4, pp. 4797–4819, 1990.
- [6] N. M. Shapiro and M. H. Ritzwoller, "Monte-carlo inversion for a global shear-velocity model of the crust and upper mantle," *Geophysical Journal International*, vol. 151, no. 1, pp. 88–105, 2002.
- [7] Y. Yang and D. W. Forsyth, "Regional tomographic inversion of the amplitude and phase of rayleigh waves with 2-d sensitivity kernels," *Geophysical Journal International*, vol. 166, no. 3, pp. 1148–1160, 2006.
- [8] A. Li and L. Li, "Love wave tomography in southern africa from a two-plane-wave inversion method," *Geophysical Journal International*, vol. 202, no. 2, pp. 1005–1020, 2015.
- [9] J. C. Babikoff and C. A. Dalton, "Long-period rayleigh wave phase velocity tomography using usarray," *Geochemistry, Geophysics, Geosystems*, vol. 20, no. 4, pp. 1990–2006, 2019.
- [10] R. B. Herrmann, C. J. Ammon, H. M. Benz, A. Aziz-Zanjani, and J. Boschelli, "Short-period surface-wave tomography in the continental united states—a resource for research," *Seismological Research Letters*, vol. 92, no. 6, pp. 3642–3656, 2021.
- [11] A. Kaviani, A. Paul, A. Moradi, P. M. Mai, S. Pilia, L. Boschi, G. Rümpker, Y. Lu, Z. Zhang, H. Yao, W. Wang, H. Zhang, H. Fang, and L. Fang, "Crustal and uppermost mantle shear wave velocity structure beneath the middle east from surface wave tomography," *Geophysical Journal International*, vol. 221, no. 2, pp. 1349–1365, 2020.
- [12] X. Xiao, L. Sun, X. Wang, and L. Wen, "Simultaneous inversion for surface wave phase velocity and earthquake centroid parameters: Methodology and application," *Journal of Geophysical Research: Solid Earth*, vol. 127, no. 9, p. e2022JB024018, 2022.
- [13] Y. Liu, Z. Yu, Z. Zhang, H. Yao, W. Wang, H. Zhang, H. Fang, and L. Fang, "The high-resolution community velocity model v2.0 of southwest china, constructed by joint body and surface wave tomography of data recorded at temporary dense arrays," *Science China Earth Sciences*, vol. 66, no. 10, pp. 2368–2385, 2023.
- [14] L. Socco and C. Strobbia, "Surface-wave method for near-surface characterization: A tutorial," *Near Surface Geophysics*, vol. 2, no. 4, pp. 165–185, 2004.
- [15] A. Mordret, M. Landès, N. M. Shapiro, S. C. Singh, P. Roux, and O. I. Barkved, "Near-surface study at the valhall oil field from ambient noise surface wave tomography," *Geophysical Journal International*, vol. 193, no. 3, pp. 1627–1643, 2013.
- [16] M. P. Barmin, M. H. Ritzwoller, and A. L. Levshin, "A fast and reliable method for surface wave tomography:," *Pure and Applied Geophysics*, vol. 158, no. 8, pp. 1351–1375, 2001.
- [17] J. Xia, R. D. Miller, and C. B. Park, "Estimation of near-surface shear-wave velocity by inversion of rayleigh waves," *Geophysics*, vol. 64, no. 3, pp. 691–700, 1999.
- [18] G. Dal Moro and M. Papan, "Joint inversion of surface wave dispersion curves and reflection travel times via multi-objective evolutionary algorithms," *Journal of Applied Geophysics*, vol. 61, no. 1, pp. 56–81, 2007.
- [19] R. B. Herrmann, "Computer programs in seismology: An evolving tool for instruction and research," *Seismological Research Letters*, vol. 84, no. 6, pp. 1081–1088, 2013.
- [20] L. V. Socco and D. Boiero, "Improved monte carlo inversion of surface wave data," *Geophysical Prospecting*, vol. 56, no. 3, pp. 357–371, 2008.
- [21] M. Maraschini and S. Foti, "A monte carlo multimodal inversion of surface waves: Monte carlo multimodal surface wave inversion," *Geophysical Journal International*, vol. 182, no. 3, pp. 1557–1566, 2010.
- [22] X. Song, L. Tang, X. Lv, H. Fang, and H. Gu, "Application of particle swarm optimization to interpret rayleigh wave dispersion curves," *Journal of Applied Geophysics*, vol. 84, pp. 1–13, 2012.
- [23] M. Sambridge and K. Mosegaard, "Monte carlo methods in geophysical inverse problems," *Reviews of Geophysics*, vol. 40, no. 3, 2002.
- [24] M. K. Sen and P. L. Stoffa, *Global Optimization Methods in Geophysical Inversion*, 2nd ed. Cambridge University Press, 2013.
- [25] Y. Li, Z. Jia, and W. Lu, "Self-supervised deep learning for 3d gravity inversion," *IEEE Transactions on Geoscience and Remote Sensing*, vol. 60, pp. 1–11, 2022.
- [26] L. Zhang, G. Zhang, Y. Liu, and Z. Fan, "Deep learning for 3-d inversion of gravity data," *IEEE Transactions on Geoscience and Remote Sensing*, vol. 60, pp. 1–18, 2022.
- [27] D. Colombo, E. Turkoglu, W. Li, E. Sandoval-Curiel, and D. Rovetta, "Physics-driven deep-learning inversion with application to transient electromagnetics," *GEOPHYSICS*, vol. 86, no. 3, pp. E209–E224, 2021.
- [28] W. Liu, H. Wang, Z. Xi, R. Zhang, and X. Huang, "Physics-driven deep learning inversion with application to magnetotelluric," *Remote Sensing*, vol. 14, no. 13, p. 3218, 2022.
- [29] F. Yang and J. Ma, "Deep-learning inversion: A next generation seismic velocity-model building method," 2019.
- [30] S. Li, B. Liu, Y. Ren, Y. Chen, S. Yang, Y. Wang, and P. Jiang, "Deep-learning inversion of seismic data," *IEEE Transactions on Geoscience and Remote Sensing*, vol. 58, no. 3, pp. 2135–2149, 2020.
- [31] R. Meier and G. Rix, "An initial study of surface wave inversion using artificial neural networks," *Geotechnical Testing Journal*, vol. 16, no. 4, pp. 425–431, 1993.
- [32] R. J. R. Devilee, A. Curtis, and K. Roy-Chowdhury, "An efficient, probabilistic neural network approach to solving inverse problems: Inverting surface wave velocities for eurasian crustal thickness," *Journal of Geophysical Research: Solid Earth*, vol. 104, no. B12, pp. 28 841–28 857, 1999.
- [33] U. Meier, A. Curtis, and J. Trampert, "Global crustal thickness from neural network inversion of surface wave data," *Geophysical Journal International*, vol. 169, no. 2, pp. 706–722, 2007.
- [34] J. Hu, H. Qiu, H. Zhang, and Y. Ben-Zion, "Using deep learning to derive shear-wave velocity models from surface-wave dispersion data," *Seismological Research Letters*, vol. 91, no. 3, pp. 1738–1751, 2020.
- [35] S. Earp, A. Curtis, X. Zhang, and F. Hansteen, "Probabilistic neural network tomography across grane field (north sea) from surface wave dispersion data," *Geophysical Journal International*, vol. 223, no. 3, pp. 1741–1757, 2020.
- [36] J. Yang, C. Xu, and Y. Zhang, "Reconstruction of the s-wave velocity via mixture density networks with a new rayleigh wave dispersion function," *IEEE Transactions on Geoscience and Remote Sensing*, vol. 60, pp. 1–13, 2022.
- [37] M. Aleardi and E. Stucchi, "A hybrid residual neural network–monte carlo approach to invert surface wave dispersion data," *Near Surface Geophysics*, vol. 19, no. 4, pp. 397–414, 2021.
- [38] Y. Gan, Z. Yang, L. Pan, Y.-C. Sun, D. Zhang, Y. Gao, and X. Chen, "Deep learning-based dispersion spectrum inversion for surface wave exploration," *IEEE Transactions on Geoscience and Remote Sensing*, vol. 62, pp. 1–11, 2024.
- [39] Y. Luo, Y. Huang, Y. Yang, K. Zhao, X. Yang, and H. Xu, "Constructing shear velocity models from surface wave dispersion curves using deep learning," *Journal of Applied Geophysics*, vol. 196, p. 104524, 2022.
- [40] A. Cai, H. Qiu, and F. Niu, "Semi-supervised surface wave tomography with wasserstein cycle-consistent gan: Method and application to south-

- ern california plate boundary region,” *Journal of Geophysical Research: Solid Earth*, vol. 127, no. 3, p. e2021JB023598, 2022.
- [41] B. Deng, J. Li, J. Liu, C. Shen, J. Suwen, and Q.-F. Chen, “The extended range phase shift method for broadband surface wave dispersion measurement from ambient noise and its application in ore deposit characterization,” *Geophysics*, vol. 87, no. 3, pp. JM29–JM40, 2022.
- [42] T. Qin, L. Lu, Z. Ding, X. Feng, and Y. Zhang, “High-resolution 3d shallow  $s$  wave velocity structure of tongzhou, subcenter of beijing, inferred from multimode rayleigh waves by beamforming seismic noise at a dense array,” *Journal of Geophysical Research: Solid Earth*, vol. 127, no. 5, p. e2021JB023689, 2022.
- [43] W. T. Thomson, “Transmission of elastic waves through a stratified solid medium,” *Journal of Applied Physics*, vol. 21, no. 2, pp. 89–93, 1950.
- [44] N. A. Haskell, “The dispersion of surface waves on multilayered media,” in *Vincit Veritas: A Portrait of the Life and Work of Norman Abraham Haskell, 1905–1970*, A. Ben-Menahem, Ed. Washington, D. C.: American Geophysical Union, 1953, vol. 43, pp. 86–103.
- [45] A. Tarantola, “Linearized inversion of seismic reflection data,” *Geophysical Prospecting*, vol. 32, no. 6, pp. 998–1015, 1984.
- [46] X. Chen, J. Xia, J. Feng, J. Pang, and H. Zhang, “Surface wave inversion using a multi-information fusion neural network,” *IEEE Transactions on Geoscience and Remote Sensing*, vol. 62, pp. 1–13, 2024.
- [47] F. Wang, X. Song, and M. Li, “A deep-learning-based approach for seismic surface-wave dispersion inversion (sfnet) with application to the chinese mainland,” *Earthquake Science*, vol. 36, no. 2, pp. 147–168, 2023.
- [48] L. V. Socco, S. Foti, and D. Boiero, “Surface-wave analysis for building near-surface velocity models — established approaches and new perspectives,” *Geophysics*, vol. 75, no. 5, pp. 75A83–75A102, 2010.
- [49] X. Chen, J. Xia, J. Pang, C. Zhou, and B. Mi, “Deep learning inversion of rayleigh-wave dispersion curves with geological constraints for near-surface investigations,” *Geophysical Journal International*, vol. 231, no. 1, pp. 1–14, 2022.
- [50] D. P. Kingma and J. Ba, “Adam: A method for stochastic optimization,” 2017.
- [51] M. E. Pasyanos, T. G. Masters, G. Laske, and Z. Ma, “Litho1.0: An updated crust and lithospheric model of the earth,” *Journal of Geophysical Research: Solid Earth*, vol. 119, no. 3, pp. 2153–2173, 2014.
- [52] T. M. Brocher, “Empirical relations between elastic wavespeeds and density in the earth’s crust,” *Bulletin of the Seismological Society of America*, vol. 95, no. 6, pp. 2081–2092, 2005.
- [53] B. L. N. Kennett, E. R. Engdahl, and R. Buland, “Constraints on seismic velocities in the earth from traveltimes,” *Geophysical Journal International*, vol. 122, no. 1, pp. 108–124, 1995.
- [54] W. Shen, M. H. Ritzwoller, and V. Schulte-Pelkum, “A 3-d model of the crust and uppermost mantle beneath the central and western us by joint inversion of receiver functions and surface wave dispersion,” *Journal of Geophysical Research: Solid Earth*, vol. 118, no. 1, pp. 262–276, 2013.
- [55] W. Shen, M. H. Ritzwoller, D. Kang, Y. Kim, F.-C. Lin, J. Ning, W. Wang, Y. Zheng, and L. Zhou, “A seismic reference model for the crust and uppermost mantle beneath china from surface wave dispersion,” *Geophysical Journal International*, vol. 206, no. 2, pp. 954–979, 2016.
- [56] X. Xiao, S. Cheng, J. Wu, W. Wang, L. Sun, X. Wang, J. Ma, Y. Tong, X. Liang, X. Tian, H. Li, Q.-F. Chen, S. Yu, and L. Wen, “Csrsm-1.0: A china seismological reference model,” *Journal of Geophysical Research: Solid Earth*, vol. 129, no. 9, p. e2024JB029520, 2024.
- [57] K. Luu, “Evdncinv: Inversion of dispersion curves using evolutionary algorithms,” Zenodo, 2023.
- [58] C. G. Lai, S. Foti, and G. J. Rix, “Propagation of data uncertainty in surface wave inversion,” *Journal of Environmental and Engineering Geophysics*, vol. 10, no. 2, pp. 219–228, 2005.
- [59] S. C. Griffiths, B. R. Cox, E. M. Rathje, and D. P. Teague, “Surface-wave dispersion approach for evaluating statistical models that account for shear-wave velocity uncertainty,” *Journal of Geotechnical and Environmental Engineering*, vol. 142, no. 11, p. 4016061, 2016.
- [60] W. P. Gouveia and J. A. Scales, “Bayesian seismic waveform inversion: Parameter estimation and uncertainty analysis,” *Journal of Geophysical Research: Solid Earth*, vol. 103, no. B2, pp. 2759–2779, 1998.
- [61] W. Shen, M. H. Ritzwoller, V. Schulte-Pelkum, and F.-C. Lin, “Joint inversion of surface wave dispersion and receiver functions: A bayesian monte-carlo approach,” *Geophysical Journal International*, vol. 192, no. 2, pp. 807–836, 2013.
- [62] F. Liu, J. Li, L. Fu, and L. Lu, “Multimodal surface wave inversion with automatic differentiation,” *Geophysical Journal International*, vol. 238, no. 1, pp. 290–312, 2024.